Three-Dimensional Characterization of Cracks in a Columnar Thermal Barrier Coating System for Gas Turbine Applications

Anne Dennstedt, Fabrice Gaslain, Marion Bartsch, Vincent Guipont, Vincent Maurel

▶ **To cite this version:**

Anne Dennstedt, Fabrice Gaslain, Marion Bartsch, Vincent Guipont, Vincent Maurel. Three-Dimensional Characterization of Cracks in a Columnar Thermal Barrier Coating System for Gas Turbine Applications. Integrating Materials and Manufacturing Innovation, 2019, 8 (3), pp.400-412. 10.1007/s40192-019-00150-7 . hal-04639135

HAL Id: hal-04639135

https://minesparis-psl.hal.science/hal-04639135

Submitted on 8 Jul 2024

HAL is a multi-disciplinary open access archive for the deposit and dissemination of scientific research documents, whether they are published or not. The documents may come from teaching and research institutions in France or abroad, or from public or private research centers.

L'archive ouverte pluridisciplinaire **HAL**, est destinée au dépôt et à la diffusion de documents scientifiques de niveau recherche, publiés ou non, émanant des établissements d'enseignement et de recherche français ou étrangers, des laboratoires publics ou privés.

Manuscript

Click here to view linked References

Click here to access/download;Manuscript;paper3DMS_Dennstendt_19042

Three-dimensional characterization of cracks in a columnar thermal barrier coating system

Anne Dennstedt[a,b], Fabrice Gaslain[a], Marion Bartsch[b], Vincent Guipont[a], Vincent Maurel[a,*]

[a] *MINES ParisTech, PSL Research University, MAT - Centre des Materiaux, CNRS UMR 7633, BP87, 91003 Evry, France*
[b] *Deutsches Zentrum für Luft- und Raumfahrt e.V. (DLR), Institut für Werkstoff-Forschung, Linder Höhe, 51170 Köln, Germany*

Abstract

Thermal barrier coatings (TBC) are multilayered systems comprising a metallic oxidation protection layer or so called bond coat (BC), a ceramic top coat (TC), and a thermally grown aluminum oxide (TGO) developing at the interface. The coating systems fail typically by delamination cracking near this interface, which has a complex three dimensional morphology influencing the crack path. This study has combined laser shock adhesion test (LASAT) to introduce an artificial interfacial crack, known in size and location and a slice and view technique based on focus ion beam slicing and subsequent imaging by a scanning electron microscope (FIB and SEM) for evaluating the crack tip. Methods for proper segmentation of cracks and adjacent materials and quantitative evaluation of the complex crack system are proposed and applied for analyzing the crack tip process zone. Finally, derived from the three dimensional segmentation, a finite element model has been achieved and used for thermal analysis highlighting the crucial role of local damage on thermal conductivity of the TBC.

Key words: Thermal Barrier Coating (TBC), Laser Shock Adhesion Test (LASAT), Focus Ion Beam (FIB), 3D imaging

Contents

*Corresponding author
Email address: vincent.maurel@mines-paristech.fr (Vincent Maurel)

1. Introduction

Thermal barrier coating (TBC) systems are applied on structural components experiencing severe thermal transients in aero engines and stationary gas turbines for energy conversion. High-pressure turbine blades, located in the first stages behind the combustion chamber, are made of nickel base superalloys. Since the gas temperatures at the turbine inlet can reach temperatures which exceed the melting temperature of nickel base superalloys, these turbine blades are internally cooled and further protected by a multilayer TBC system comprising a ceramic top coat (TC) for thermal insulation and a metallic coating, the so-called bond coat (BC), for protection against oxidation and improving the adhesion of the TC. Materials for the metallic BC are alloys with a high aluminum content to provide a reservoir of aluminum for forming a dense alumina layer acting as a diffusion barrier for oxygen, the so-called thermally grown oxide (TGO). The TC is typically zirconia, partially stabilized with 6 - 8 wt. % yttria (YSZ). The ceramic layer is highly porous for providing a low thermal conductivity of about 1 - 2 W/m/K [1, 2]. The coating system has to sustain high temperatures and stresses induced by mechanical loads and transient thermal gradients. Optimization of materials composition and processing aims at limiting the coefficient of thermal expansion (CTE) mismatch in such a heterogeneous multi-layered system. For extremely severe conditions YSZ is processed by electron beam physical vapor deposition (EB-PVD) taking advantage of lower stress induced by the lower stiffness offered by the columnar morphology as compared to coatings applied by the air plasma spray (APS) process. This study is focused on EB-PVD YSZ. However, degradation occurs during service leading to damage accumulation, crack initiation and growth, mostly located at the interfacial region near the TGO under thermal cycling or thermo-mechanical fatigue loading [3–5]. Finally, interfacial cracking, being a delamination mechanism, leads to a sequence of blistering and spallation of the TC. Comprehensive overviews over loading conditions and damage mechanisms of TBC systems can be found for example in [1, 6]. Interfacial degradation mechanisms have been widely documented mainly based on observation on cross sections processed by saw or wire-cutting, providing only two dimensional (2D) information of the interface and damage morphology. However, the precise 3D information of the interface morphology and the size and location of cracks has to be addressed since the size and morphology of the so-called process zone of a crack modifies the available strain energy density for final buckling and subsequent spallation [7]. Further, the 3D characterization of the interfacial region is important to gain understanding of the role of interfacial morphology and damage in thermal protection, since the thermal conductivity is known to be a direct function of the interfacial morphology [8]. On one hand, X-ray computed tomography (CT) and computed laminography (CL) have appeared to be attractive methods to establish the target interface 3D morphology [9, 10]. CT is limited to very small TBC specimens - rods of less than 500 μm in diameter, when the TBC is applied on Ni base superalloy substrate [11]. CL, which is similar to CT but with a different X-ray beam angle to the specimens rotational axis (90° for CT and typically 60° for CL) enables to analyze a large plate with in plane extension in the centimeter range [12]. Applied to TBC, CL has provided clear evaluation of progressive damage with thermal cycling [13]. The drawback of CT and CL is the limited spatial resolution of about 100 - 500 nm for CT and a few μm for CL limiting its applicability to macroscopic evaluation of 3D evolution of TBC damage. On the other hand, the slice and view technique combining focus ion beam (FIB) cutting with a scanning electron microscope (SEM), enables by 3D image analysis to obtain details of a complex microstructure. Further, this method is gentle and even brittle and weakly bonded materials as the TGO on bare oxidized alloys are preserved [14]. After 3D reconstruction, the spatial resolution is in the range of about 2 - 20 nm, depending on the distance between the FIB slices. Moreover, FIB has been successfully applied to a TBC to obtain thin foils for transmission electron microscopy [15]. Thus, the FIB-SEM slice and view technique is an attractive method for studying details of a 3D TBC morphology.

In the wide range of mechanical testing to characterize interfacial adherence, laser adhesion test (LASAT) is a promising technique [16]. It features the application of a laser shock on the coating system to be evaluated, and using a confinement media, laser to mater interaction yields the fast expansion of plasma generated at the targeted surface which produces a compressive wave propagating in the system to the free interface where it becomes a tensile wave. If the tensile stress induced by the shock wave exceeds the

local toughness (at the interface or at the weak points in a coated system) it results in local cracking [17]. Recent progress in LASAT has enabled for the first time to obtain clear ranking of adherence quality as a result of processing conditions in both as-processed condition and after thermal cycling, even the evolution of adherence with thermal cycling has been evaluated [18]. The chosen methodology is used in this case to establish 2D-LASAT curves by varying the laser power density to determine both the so-called LASAT threshold, namely the minimum laser power density to induce delamination, and the evolution of the size of debonded area as a function of the laser power density beyond this threshold value. The second methodology derived from LASAT aims at the introduction of an artificial debonded disk known in size and location in the coated system. These techniques were applied both for further mechanical testing [19] and thermal cycling [18, 20]. The major interest of such a methodology is to determine precisely the locus point of examination. Besides, it has been shown by cross-sectioning that the damaged interface by LASAT in EB-PVD TBC was mainly the TC/TGO interface.

The aim of this study is to obtain a precise characterization of the near crack tip 3D morphology in a typical EB-PVD TBC system. The chosen approach is based on the combination of LASAT to process an artificial interfacial defect and the FIB slice and view technique at the process zone near the crack tip obtained.

2. Experimental

2.1. Sample and generation of artificial defects

The studied TBC system is applied on a 2 mm thick IN718 superalloy substrate with 2 cm x 2 cm in plane dimensions, and comprises a 50 μm BC deposited by a diffusion coating process and a 150 μm thick yttria stabilized zirconia (7 wt% Y2O3) TC deposited via an EB-PVD process. LASAT is used to generate a nearly circular interfacial defect. The substrate side of the sample was exposed to the laser, and confinement of the laser is achieved through covering of the substrate side by a transparent adhesive tape. The laser used is set to 5.2 ns and λ= 532 nm. The set-up induces a shock wave diameter of 2.56 mm. During the series of laser shocks in this experiment, the energy of the laser was decreased until no delamination was detected after the laser shock. Details of energies and flux can be found in Table 1.

2.2. Macroscopic inspection of artificial defects

Visual inspection of the coating after the laser shock experiment can give evidence of the damages: at the created delamination the coating looks brighter than at the undamaged regions. The white color of the coating is unchanged if there is no delamination. In contrast, a spallation of the TC exposes dark regions of the underlying material [21]. Alternatively, the sample is put with the metallic substrate onto a heating plate set to 50 °C while the temperature change is monitored by an IR camera (Titanium 520SB GeminiBB MW F/3 (InSb) with a 320 x 256 pixel large detector). This thermography method yields a cold region when there is an interfacial crack limiting the heat flow from the substrate to the ceramic coating [19, 20]. The thermography was used in this study.

2.3. Microscopic investigation of delamination and crack tip region

After this first investigation, the sample with the LASAT delaminations was embedded in transparent resin (SpeciFix, Struers) for preparing a cross section through the delamination cracks. The embedding process was performed under vacuum for infiltrating the porous TC and the part of the delamination crack connected via gaps and open porosity of the TC to the surface. The infiltration conserves the crack system generated by LASAT and avoids further damage during subsequent sample preparation by grinding and polishing. The region of interest is the process zone at the crack tip. Image stacks for further reconstruction of 3D images of the crack tip region were processed by means of a dual beam microscope providing a focused ion beam for cutting the sample and an electron beam for subsequent imaging (HELIOS NANOLAB 660, FEI). Prior to the slice and view procedure on the region of interest this area has been covered by an approximately 2 μm thick carbon layer by ion beam deposition. This thick carbon layer reduces damage associated with the FIB cutting process. Further, the adjacent material was removed by the ion beam

generating a groove of about 10 - 20 μm, which provides space for material to be removed in the subsequent slicing process and allows accessing the cut surface by SEM. During the subsequent slice and view procedure, images by both secondary electron (SE) and back- scattered electron (BSE) detector were collected, in order to achieve images with complementary contrast for properly discerning TGO, BC, TC, and voids, such as cracks and pores. The incremental FIB cutting was performed in a region containing the process zone of the propagating crack near the crack tip. About 24 μm were removed in steps of 20 nm. Two image stacks are obtained during FIB slice and view procedure, each image with a dimension of 1536 x 1024 pixels. Further image processing had to be performed before achieving quantitative values of the reconstructed volume. First, the images are corrected in pixel size as well as in the alignment. The alignment correction is performed using the plugin "Align slices in stack" in Image J [22]. Thereafter, image regions not showing the sample surface were removed by cropping the images to a size of 550 x 710 pixels. The last step in Image J was the enhancement of the contrast in each image. For subsequent analyses stacks with 944 images were used. Further method and image analysis are described below.

3. Results

3.1. 2D Observations

Three laser shocks have been used to produce defects within the TBC system. Two experiments resulted in a clear detectable decohesion, while in the third experiment the laser flux was below the LASAT delamination threshold, see thermography images in the inset of Fig. 1. In this image the arrows indicate the positions of the three laser shocks corresponding to a decreasing energy from the right to the left; the delamination diameter estimated by thermography is plot as function of the applied laser flux. Fig. 2a shows an SEM image taken in BSE mode of the TBC cross-section of the delamination chosen in this study for investigation (right delamination in Fig. 1). In this cross-section, decohesion induced by LASAT was measured as 2 mm in length, and the TC, TGO, and BC thicknesses were of about 150, 1, and 50 μm, respectively. The columnar morphology of the EB-PVD TC displays typical variation in column width and so-called "pinched off" defects of different size [23, 24]. Because of the laser shock, some small dense pinched off regions are detached from the delaminated ceramic layer, staying attached to the TGO. The accidental central defect within the ceramic layer, visible in Fig. 2a, is far enough from the crack tip not to generate any artifact on the morphology of the crack tip process zone. Further SEM investigations at higher magnifications verified that gaps and cracks in the TC and TC-TGO interfacial region are well infiltrated by the resin, confirming that the observed cracks were generated before sample preparation. Because this cross-section image was collected after the FIB-slice and view procedure, the position of the volume extracted is visible in the left part of the image. The position was chosen to have a volume that contains parts of ceramic coating, TGO, and bond coat as well as the crack tip process zone, Fig. 2b. Fig. 3a and b show examples of the BSE and SE SEM images, respectively that are collected during the FIB slice and view procedure. Both images show the same slice surface, BSE image highlighting contrast in composition, which is helpful for discerning different phases, and SE image highlighting contrasts in morphology, which is helpful for crack analysis. In BSE mode, the TGO appears dark and it is difficult to differentiate between cracks and TGO. In SE mode cracks appear darker than the TGO which allows discerning both.

3.2. FIB-SEM 3D images and segmentation

The aligned stack of BSE images is shown in Fig. 4a. Four virtual cross sections of the TC are shown in Fig. 4b. The colored lines in Fig. 4a indicate the positions of the different virtual cross sections by their colored frames. These cross sections of the ceramic coating show both the columns of the ceramic in bright gray as well as in dark gray the gaps between the columns. In the cross sections near to the BC (red and blue frame) larger dark colored areas occur in addition to the fine dark lines indicating the gaps between the columns. These areas are related to the crack system at the TC-TGO interface. The combination of all resin or air filled regions in the TC and at the interfaces within the TBC system is called voids and is estimated as one phase during the segmentation procedure described in the following. Moreover, internal porosity due to the feather-like structure of columns is visible in Fig. 3 and appears blurred in Fig. 4a.

The size of intra-columnar pores is in the nanometer to sub-micrometer range and will not be detailed in the sequel [25]. However, FIB allows clearly identifying this kind of feature. Besides, no evidence of damage induced by the FIB slice and view technique has been observed.

In AVIZO [26], firstly, a three-dimensional median filter is applied to both image stacks that are loaded with a voxel size of 20 x 20 x 20 nm3. Thereafter, the segmentation procedure starts, as explained in Fig. 5. For the segmentation both image stacks shown in Fig. 5a are used. In a first step, the regions which are dark grey in the BSE and the SE image stack as well are assigned to BC (Fig. 5b). The second step is the assignment of the YSZ TC (Fig. 5c), which appears bright in SE and BSE mode as well. The remaining voxels have to be assigned either to TGO or to voids. In the SE image stack shown in the right part of Fig. 5c, these two regions can be differentiated very well because the TGO appears as bright voxels whereas the voids appear as dark voxels. Thus, with this last step, the assignment shown in Fig. 5d is obtained. The BC is shown in red, the TGO as light blue, the voids in green, and the voxels of YSZ are left transparent to give a view to the distribution of the voids in the volume. After this segmentation procedure, each voxel is assigned to one of the four phases.

3.3. Qualitative phase and void analysis

The aim of this study is to determine precisely the shape of cracks within the complex morphology of the TBC system. It is thus straightforward to isolate the oxide layer and voids, highlighted in blue and green, respectively in Fig. 6. In the sequel top view refers to view from TC side, whereas bottom view refers to view from the BC side; consistently, above and below TGO correspond respectively to TGO/TC and BC/TGO interfaces. The side and top views show the difficulty inherent to the fact that interfacial crack and inter-columnar voids are segmented in a single phase, Fig. 6 a and b. However, at the TGO layer the interfacial crack can be discerned from the inter-columnar gaps when it is between TGO and BC (Fig. 6c) and when it is crossing the TGO layer (Fig. 6b). Assuming that the interfacial crack is mainly oriented parallel to the interface and following the crack path from the BC/TGO interface through the TGO also some part of the void volume between TGO and TC can be assigned to the interfacial crack, being above (see labels 1 and 3) and below the TGO (see label 2), Fig. 6b (see also Fig. 5d). From the top-view (Fig. 6a), crack and gap areas are visible, but with different features, which can be identified if comparing different views. Some void volumes are clearly part of the interfacial crack area above the TGO (labels 1 and 3), some others belong to cracks located within the TC but are oriented parallel to the interface (label 4), Fig. 6a and b. Besides, the areas showing the TGO surface (blue color) represent the intact interfaces between either BC and TGO (bottom view in Fig. 6 c) or TGO and TC (top view in Fig. 6 a, label 5). Void volumes belonging to structures with planes oriented perpendicular to the interface are visible in the side view (Fig. 6b) and belong to the inter-columnar gaps. The dynamic rotation of this image facilitates these interpretations and can be found as supplementary material on the website of the journal. To get more into details, phase volume fraction analysis was performed for planes perpendicular to the coating thickness extension.

3.4. Quantitative phase and void analysis

The chosen approach for a quantitative characterization of the interfacial region and especially the crack system is described in Fig. 7. The segmented volume is shown in Fig. 7a using the same colors as before (Fig. 5 and 6) and further the positions of the virtual cross sections are given which are shown in Fig. 7b. In the sections the ceramic coating is represented as dark grey area. In addition, Fig. 7a displays an arrow indicating the numbering direction of the cross section images. The first images to be analyzed are located at the bottom of the volume; they contain completely the BC phase. But, already in virtual cross section # 1, shown in Fig. 7b, fractions of TGO and void phase are visible. The virtual cross section #2 contains all four phases that were assigned before. The virtual cross section #3 shows the YSZ as dominant phase, but also some voids are visible due to the inter-columnar gaps in the TC. A phase fraction analysis of all single virtual cross sections is processed to get quantitative information from this 3D image. A plot showing the phase fractions as function of the location represented by the image number is presented in Fig. 7c, using red, blue, dark grey and green as in Fig. 7a and b. Near to the bottom plane of the reconstructed volume,

corresponding to low image numbers, BC phase is prevailing. With increasing image number, corresponding to an increase in the distance from the bottom plane of the reconstructed volume, firstly a phase fraction of TGO occurs and increases from the first BC/TGO interfacial point (at image #33) up to a maximum value corresponding to the average distance of the TGO voxels from the bottom plane (at image #154) and decreases down to zero at the last interfacial TGO/TC contact (at image #235). On the other hand, BC phase fraction decreases progressively from the first plane where TGO appears and reaches a value of zero at image #179. Conversely, the TC phase fraction increases from the first interfacial TGO/TC contact (at image #92) to reach a phase fraction above 90% (at image #230). The void phase fraction combines crack and inter-columnar gaps as described above. Firstly, phase fraction of voids increases from the first voxel assigned to an interfacial crack between BC and TGO (at image #72) up to a maximum value of 21% (at image #177) corresponding to the average distance of the interfacial crack induced by LASAT to the bottom plane. Further, the void volume fraction decreases to less than 3% (at image #399) where only inter columnar gaps are present. The maxima of TGO and void volume fraction are shifted with the maximum of the TGO volume fraction located closer to the bottom plane, indicating that cracking occurs predominately between TGO and TC. However, due to the relatively large volume analyzed, phase distributions of the different phases appear as (more or less) broad peaks, limiting clear localization of phases and interfacial cracks.

In order to get more precise local information about the spatial distribution of phase fractions and crack path of interfacial cracks, the volume is divided into 12 sub-volumes adjacent to each other (i.e. without any overlapping). Each of this sub-volumes has the same size (4.5 μm times 4.5 μm and a height of 10.8 μm). They are shown in Fig. 8 with some spaces in between to provide a better view to phase distributions in the single volumes. Already in this figure, differences between the different sub-volumes can be seen. Each of these sub-volumes was evaluated in the way described before. The resulting phase fractions are shown in Fig. 9.

The plots of the single sub-volume show significant differences, which are not discernible if the entire volume is evaluated. For example, in four sub-volumes the maximum of crackVoid volume fraction occurs more close to the BC than the respective maximum of the TGO phase, indicating interfacial crack at the BC/TGO interface, while by averaging only the presence of some crack volume before considerable volume fraction of TC material occurs, indicates cracking either at the BC/TGO interface or within the TGO. In different sub-volumes also the width of the volume fraction distribution of crackVoid and/or TGO can differ significantly, providing quantitative information on the amplitude of interface roughness. Further, some plots in Fig. 9 display isolated maxima of void volume within in the TC corresponding with a minimum of YSZ (sub-volumes 1, 2, 4, 7, and 10). These maxima can be associated to cracks parallel to the coating plane.

For analyzing the path of delamination cracks, the interfacial region along BC/TGO and TGO/TC interfaces is characteristic while contact areas between voids and the YSZ of the TC can either be part of an interfacial delamination crack or part of the inter-columnar gaps within the TC. Focusing on the interfacial region, four phases are involved, BC, TGO, YSZ (TC), and crack. Due to the layered structure of the coating system five types of interface can emerge between these four phases: BC-CrackVoids, BC-TGO, TGO-CrackVoids, TGO-YSZ, and YSZ-CrackVoids. The area of the different interfaces can be extracted from the respective virtual sub-volume. In Fig. 10 the different interface areas of all sub-volumes are summarized. By comparing the areas and fractions of their different interface types the sub-volumes can be assigned to three groups: (1) considerable fraction of cracks between BC and TGO with correspondingly reduced intact interface area between BC and TGO (sub-volumes 5, 6, 8, and 9); (2) no considerable cracking between BC and TGO but between TGO and YSZ (sub-volume 4, 11, and 12); (3) no considerable cracking neither between BC and TGO nor between TGO and YSZ but contact areas between YSZ and voids (sub-volumes 1, 2, 3, 7, and 10). As mentioned before, comparing the interfacial areas between YSZ and voids provides limited information about the interfacial crack path, since the ceramic TC has a priori a large interface to CrackVoids because of its columnar microstructure. However, it is eye-catching that in group one the interfacial area between YSZ and CrackVoids is relatively small. In Fig. 10 the graphs belonging to one group are plotted in the same color, and assignment of sub-volumes to these three groups is highlighted by associated background colors in the plots of Fig. 9. The results derived from the phase fraction analysis

and analyses of the interfacial areas can be used to describe the process zone near the crack tip. Further, with the clear segmentation of YSZ, TGO, BC, and voids, achieved by the FIB slice and view technique, geometry models for finite element (FE) calculations can be generated and directly meshed by means of the AVIZO toolbox. An example for a thermal analysis on a sub-model of the virtual volume from the FIB slice and view procedure will be given in the discussion.

4. Discussion

4.1. Crack tip process zone

Considering the location of sub-volumes with the global debonded area by LASAT is of interest, Fig. 2b. At the global level the crack could be viewed to "enter" and "exit" the volume worth of investigation, namely the crack enters sub-volume #1, along the side #1, 2, 3 (or corner #1, 2, 4), and exits on #12, along the corner (#9, 11, 12). Consistently, the associated voids distribution is larger on crack enter (sub-volumes #1, 2, 3 in Fig 9) than on crack exit (sub-volumes #11, 12 in Fig 9). This could be induced by local increase in roughness, but should be observed together with the TGO distribution. Because, the span of TGO distribution is almost constant when comparing enter and exit location, it appears that the crack is more opened when entering than when exiting the volume analyzed.

The crack induced by LASAT was observed to be mainly located at the TGO/TC interface, but the crack path changes to some extent from the TGO/TC interface to the BC/TGO interface, compare Fig. 6 a - c. The change of interface during crack propagation is associated to undulations of the TGO (Fig. 6b and c). If the interfacial fracture toughness of the two involved interfaces is not very different, it is likely that crack propagation in Mode I needs less energy than following the curved interface, even if the TGO layer has to be fractured. Besides, some cracks can be observed within the TC. This result is consistent with former results of LASAT damage in TBC-systems since the tensile shock wave damages the weakest part of the system [18, 21]. Following the crack propagation direction from the sub-volumes 1, 2, and 3 to corresponding sub-volumes 10, 11, and 12, crack branching occurs, and at some locations the crack deviates into the TC where parts of the crack end up coalescing with the inter-columnar gaps, which in this cases seem to act like "crack traps". It can be concluded that the 3D imaging allows for observing and evaluating mechanisms of energy dissipation in the process zone near the crack tip and how they are influenced by the morphology of TGO (roughness) and TC (columnar structure with gaps, orientation of gaps).

It is plausible that besides the microstructure of TGO and TC the applied load, e.g. mode I or mode II with respect to the crack orientation plays a considerable role on the characteristics of the crack tip process zone. Using LASAT for introducing delamination cracks and further targeted FIB slice and view processing was straightforward, since the location of the delamination crack is quite easy to determine, lateral and in depth of the coating system. Further, the loading conditions for a delamination crack are well known. The LASAT tensile shock wave generates delaminations with a diameter exceeding the initial laser shock diameter. Thus, some lateral growth has occurred during LASAT, that corresponds to the so-called 2D effect in LASAT [27] associated to a buckling-driven delamination process of debonding from LASAT [28]. On the other hand, the FIB slice and view technique can be used to elucidate process zone characteristics of cracks in TBC systems which have been introduced by other methods than LASAT or which occur in coated components during service in turbine engines.

4.2. Local conductivity

Because a clear segmentation of YSZ, TGO, BC and voids has been achieved within this work, direct meshing of individual phases for generating FE-models can be performed using the AVIZO toolbox. As a first example, it has been evaluated how a thermal flux will be modified by the presence of a complex but realistic 3D model of interfacial damage. This has been achieved using the Zset code [29] for transient thermal analysis. The chosen meshed volume corresponds nearly to sub-volume 8 using 293168 linear reduced tetrahedron elements leading to 54915 degrees of freedom, Fig. 11a. Heat flux has been prescribed at both top and bottom sides of the meshed volume, corresponding respectively to TC and BC, whereas thermal flux is set to zero on the four remaining external planes of the model. The thermal properties of each phase are

summarized in Table 2. Two cases have been analyzed. Case A / IRT condition corresponds to the condition used for infrared thermography (IRT): at the BC heat flux is prescribed with an external temperature (Te) set to 50 ° C, whereas the TC side is cooled to RT and Te set to 20 ° C. Case B / HT condition corresponds to representative high temperature gradient condition for internally cooled components: at the TC side heat flux is prescribed with Te set to 1000 ° C, whereas at the BC side Te is set to 700 ° C. Cases A and B have been modeled using distinct thermal properties for each phase, BC, TGO, YSZ, and voids, including cracks and inter-columnar gaps considered as air, referred as to "Voids" in the sequel. For case A / IRT condition, the resulting temperature field shows that the presence of the complex interfacial crack strongly modifies the thermal flux (Fig. 11a). The most affected zone appears to be the ceramic TC layer, whereas the higher conductivity of the metallic BC leads to a short range influence of interfacial defect. For the chosen sub-volume, the amplitude of interface roughness is about 1.3 μm. The area of thermal flux modification is about 2.8 μm in height, for a crack opening of about 200 nm. To get more into details, cases A and B have been analyzed along a set of points crossing each layer (BC, TGO, crackVoids, and TC), highlighted in black in Fig. 11b and c. The temperature field calculated for case A is displayed in Fig. 12b. Besides, for comparison purpose, cases A and B have been modeled using distinct thermal properties for each phase, BC, TGO, and YSZ, but considering cracks and inter-columnar gaps as YSZ, referred as to "Filled". For Filled condition, the obtained gradients correspond to a reference case where temperature gradients arise from bulk properties of each phase, BC, TGO, and YSZ for case A and B thermal tests. Fig. 11c displays the temperature field for the case A with "filled condition". In this case, the transition of thermal properties within the TGO slightly modifies the iso-lines of temperature, but they remain almost parallel to each other. In the presence of voids, a considerable temperature jump is evidenced when crossing the crack and smaller temperature jump when crossing the TGO, for both cases A and B, compare Fig. 12a and b, respectively. Besides, it appears that the thermal inertia is modified by the presence of voids, since the temperatures at top and bottom of the model are slightly modified increasing the global temperature difference in presence of a crack. In case B / HT condition, the TC is globally hotter in presence of a crack than considering the filled condition, Fig. 12b. This is consistent with an acceleration of HT damaging when interfacial cracking already exists. It has been observed that when interfacial crack occurs, the increase of TGO/BC roughness, the so-called rumpling mechanism, can take place due to lesser constraint between BC/TGO and TC. In this context, it has been recently shown for a TBC system that, when an interfacial crack precedes further thermal cycling, the BC area lying within the cracked area shows higher level of rumpling as compared to areas with adherent coating [18], in this case higher local temperature can increase the local effect of free surface in rumpling. In case A / IRT condition, the TC surface is colder in presence of an interfacial crack than considering the filled condition, Fig. 12a. This is consistent with IRT measurement where debonded areas correspond to colder areas measured from the topside, compare insert in Fig. 1.

5. Conclusions

This work has proposed an original methodology using LASAT to introduce an interfacial defect in a TBC system. By knowing the defect size and localization, a targeted FIB-SEM slice and view 3D preparation has been processed. The resulting virtual volume containing a part of the near crack tip process zone has been analyzed. Main results can be resumed as follows:

- FIB-SEM slice and view technique is a straightforward method to generate virtual volumes for analyzing local interfacial damage in a TBC system without introducing further damage;
- The use of both SE and BSE modes has enabled to obtain a clear segmentation of each constitutive phase of the damaged TBC, namely YSZ, TGO, metallic BC and voids;
- A systematic analysis of phase fraction along the thickness of the observed volume and an quantitative analysis of different types of interface areas has enabled to localize the crack within different phases and along different interfaces;

- Finally, FIB-SEM observation and subsequent segmentation of phases have enabled to estimate the role of interfacial damage on local conductivity, showing the large impact of a very local debonding in TBC thermal properties.

Acknowledgement

Part of this work was carried out within the MATMECA consortium and supported by the ANR under contract number ANR-10-EQUIPEX-37 14. Further, we acknowledge funding by the German Science foundation under contract SFB TRR 103, project A3. A.D. thanks the Zuse Institute Berlin (ZIB) for access to the AVIZO software and for fruitful discussions.

Conflict of interest

On behalf of all authors, the corresponding author states that there is no conflict of interest.

List of tables and captions

Table 1: Parameters of the three LASAT experiments

Table 2: Thermal properties for FE- analyses (from [30] for YSZ, TGO and BC properties and from [31] for air properties).

List of figures and captions

Figure 1: Measurement of the debonded diameter as a function of laser flux; insert shows a temperature field obtained by infra-red thermography (IRT) after LASAT. (Temperatures are defined by the assigned color)

Figure 2: (a) Micrograph of the sample cross section by scanning electron microscopy using a backscatter electron detector (BSE) (b) Location of the virtual volume extracted by means of FIB slice and view process. The numbers 1 to 12 refer to individually analyzed sub-volumes (compare Figs. 8 - 10)

Figure 3: SEM micrographs displaying a snap-shot of a slice from the region of interest during progressive FIB-slicing in (a) BSE mode and (b) SE mode.

Figure 4: Reconstructed volume from FIB slice and view process, (a) perspective 3D view and (b) view of slices parallel to the coating plane.

Figure 5: Segmentation methodology with subsequent processing steps. (a) Image stack of slices in BSE-mode (left) and SE-mode (right), (b) assigning volumes, which are dark grey in BSE and SE-mode as well to BC (in red), (c) assigning volumes shown bright in BSE and SE as well to YSZ- TC (dark blue), (c) segmentation of the remaining volume by means of the SE image into TGO (bright grey) and void (dark grey), (d) all volumes assigned (BC in red, TGO in bright blue, inter-columnar gaps in green, and the TC transparent to allow for viewing the structure of inter-columnar gaps).

Figure 6: Segmented TGO (dark blue) and voids (green), (a) top-view, (b) side-view, and (c) bottom view.

Figure 7: (a) Perspective view of the virtual volume achieved by FIB slice and view with TGO (dark grey) and voids (green) where sections 1 to 5 have been superimposed, (b) top-view of associated sections 1 to 5, and (c) phase volume fractions along the direction of image numbering starting from the BC towards the TC.

Figure 8: TGO (blue) and voids (green) in 12 sub-volumes of the entire segmented volume

Figure 9: Phase fraction analysis as derived from the 12 sub-volumes of the FIB-sliced volume as displayed in Fig. 8 with image numbering starting in each diagram from BC towards TC. The sub-volumes are assigned to three groups (compare Fig. 10), indicated by colored background: group 1 with red background (sub-volumes 5, 6, 8, 9), group 2 with green background (sub-volumes 4, 11, 12), and group 3 with blue background (sub-volumes 1, 2, 3, 7, 11).

Figure 10: Fractions of different interface areas in the sub-volumes of Fig. 8. Due to characteristics in the distribution of interface area fractions, 3 groups of sub-volumes were defined as indicated by the colors. The same colors are used as background color in Figure 9 indicating to which group the respective sub-volume belongs.

Figure 11: (a) Meshed FE-Model of a sub-volume from the virtual volume extracted by FIB slice and view process with an overview of the temperature distribution for case A / IRT condition, (b) vertical slice of the model showing the temperature field for the case of air filled voids (interfacial cracks and inter-columnar gaps in the TC) superposed to the element sets in the mesh corresponding to (from the bottom to top) BC, TGO, crack, and YSZ with vertical gap, (c) the same vertical slice but the temperature field corresponding to the case of YSZ filled cracks and gaps.

Figure 12: Temperature evolution from FEA extracted along a vertical line at points highlighted in black in Fig 11(b) and (c); (a) temperature distribution for case A / IRT condition, (b) temperature distribution for case B / HT condition. "Voids": air properties in voids and "Filled": YSZ properties in voids

Bibliography

References

[1] A. G. Evans, D. R. Mumm, J. W. Hutchinson, G. H. Meier, and F. S. Pettit. Mechanisms controlling the durability of thermal barrier coatings. *Progress in Materials Science*, 46(5):505 – 553, 2001.

[2] John R Nicholls, KJ Lawson, A Johnstone, and DS Rickerby. Methods to reduce the thermal conductivity of eb-pvd tbcs. *Surface and Coatings Technology*, 151:383–391, 2002.

[3] N. Yanar, F. Pettit, and G. Meier. Failure characteristics during cyclic oxidation of yttria stabilized zirconia thermal barrier coatings deposited via electron beam physical vapor deposition on platinum aluminide and on nicocraly bond coats with processing modifications for improved performances. *Metallurgical and Materials Transactions A*, 37(5):1563–1580, 2006.

[4] Marion Bartsch, Bernd Baufeld, S. Dalkiliç, L. Chernova, and Michael Heinzelmann. Fatigue cracks in a thermal barrier coating system on a superalloy in multiaxial thermomechanical testing. *International Journal of Fatigue,*, 30(2):211–218, 2 2008.

[5] MT Hernandez, D Cojocaru, M Bartsch, and Anette M Karlsson. On the opening of a class of fatigue cracks due to thermo-mechanical fatigue testing of thermal barrier coatings. *Computational Materials Science*, 50(9):2561–2572, 2011.

[6] ZA Chaudhury, GM Newaz, SQ Nusier, T Ahmed, and RL Thomas. Chronological evaluation of interfacial damage in tbc due to thermal cycling. *Journal of materials science*, 34(10):2475–2481, 1999.

[7] Pablo D Zavattieri, Louis G Hector Jr, and Allan F Bower. Cohesive zone simulations of crack growth along a rough interface between two elastic–plastic solids. *Engineering Fracture Mechanics*, 75(15):4309–4332, 2008.

[8] MP Bacos, JM Dorvaux, S Landais, O Lavigne, R Mévrel, M Poulain, C Rio, and MH Vidal-Sétif. 10 years-activities at onera on advanced thermal barrier coatings. *AerospaceLab*, (3):p–1, 2011.

[9] J-Y Buffiere, E Maire, J Adrien, J-P Masse, and E Boller. In situ experiments with x ray tomography: an attractive tool for experimental mechanics. *Experimental mechanics*, 50(3):289–305, 2010.

[10] L. Helfen, T. Baumbach, P. Pernot, P. Mikulík, M. DiMichiel, and J. Baruchel. High-resolution three-dimensional imaging by synchrotron-radiation computed laminography. *Proc. SPIE*, 6318:63180N, 2006.

[11] D Khoshkhou, M Mostafavi, C Reinhard, MP Taylor, DS Rickerby, IM Edmonds, HE Evans, TJ Marrow, and BJ Connolly. Three-dimensional displacement mapping of diffused pt thermal barrier coatings via synchrotron x-ray computed tomography and digital volume correlation. *Scripta Materialia*, 115:100–103, 2016.

[12] T.F. Morgeneyer and J. Besson. *Scripta Materialia*, 65(11):1002 – 1005, 2011.

[13] V. Maurel, R. Soulignac, L. Helfen, T.F. Morgeneyer, A. Koster, and L. Remy. Three-dimensional damage evolution measurement in ebpvd tbc using synchrotron laminography. *Oxidat. of Metals*, 79(3-4, SI):313–323, 2013.

[14] Cécilie Duhamel, Jacqueline Caballero, Thierry Couvant, Jérôme Crépin, Fabrice Gaslain, Catherine Guerre, Hong-Thaï Le, and Mickaël Wehbi. Intergranular oxidation of nickel-base alloys: potentialities of focused ion beam tomography. *Oxidation of Metals*, 88(3-4):447–457, 2017.

[15] AJ Burns, R Subramanian, BW Kempshall, and YH Sohn. Microstructure of as-coated thermal barrier coatings with varying lifetimes. *Surface and Coatings Technology*, 177:89–96, 2004.

[16] Xiaomei Chen, Christopher Shaw, Len Gelman, and Kenneth TV Grattan. Advances in test and measurement of the interface adhesion and bond strengths in coating-substrate systems, emphasising blister and bulk techniques. *Measurement*, 2019.

[17] V Gupta, AS Argon, JA Cornie, and DM Parks. Measurement of interface strength by laser-pulse-induced spallation. *Materials Science and Engineering: A*, 126(1-2):105–117, 1990.

[18] Vincent Guipont, Geoffrey Begue, Gregory Fabre, and Vincent Maurel. Buckling and interface strength analyses of eb-pvd tbc combining laser shock adhesion test (lasat) to thermal cycling. *Surf. Coat. Technol.*, under review(special issue 46th ICMCTF), 2019.

[19] Hélène Sapardanis, Vincent Maurel, Alain Köster, Steve Duvinage, François Borit, and Vincent Guipont. Influence of macroscopic shear loading on the growth of an interfacial crack initiated from a ceramic blister processed by laser shock. *Surface and Coatings Technology*, 291:430–443, 2016.

[20] Melanie Theveneau, Vincent Guipont, Basile Marchand, Florent Coudon, and Vincent Maurel. Damage monitoring and thermal cycling life of thermal barrier coating involving lasat (laser shock adhesion test). *Surf. Coat. Technol.*, under review(special issue 46th ICMCTF), 2019.

[21] G. Fabre. *Influence des propriétés optiques et de l'endommagement de barrières thermiques EB-PVD pour la mesure d'adhérence par choc laser LASAT-2D (in French).* PhD thesis, Mines ParisTech, 2013.

[22] Linear stack alignment with sift. https://imagej.net/$Linear\_Stack\_Alignment\_with\_SIFT\#cite\_ref-1$. Accessed: 2019-04-22.

[23] D. R. Mumm, A. G. Evans, and I. T. Spitsberg. Characterization of a cyclic displacement instability for a thermally grown oxide in a thermal barrier system. *Acta Materialia*, 49(12):2329 – 2340, 2001.

[24] Anette M Karlsson, T Xu, and AG Evans. The effect of the thermal barrier coating on the displacement instability in thermal barrier systems. *Acta Materialia*, 50(5):1211–1218, 2002.

[25] N Zotov, M Bartsch, and G Eggeler. Thermal barrier coating systems analysis of nanoindentation curves. *Surface and Coatings Technology*, 203(14):2064–2072, 2009.

[26] Avizo for materials science. https://www.thermofisher.com

[27] Geoffrey Bégué, Grégory Fabre, Vincent Guipont, Michel Jeandin, P Bilhe, Jean Yves Guedou, and François Lepoutre. Laser shock adhesion test (lasat) of eb-pvd tbcs: Towards an industrial application. *Surface and Coatings Technology*, 237:305–312, 2013.

[28] S Faulhaber, C Mercer, M-W Moon, JW Hutchinson, and AG Evans. Buckling delamination in compressed multilayers on curved substrates with accompanying ridge cracks. *Journal of the Mechanics and Physics of Solids*, 54(5):1004–1028, 2006.

[29] Zset software, non-linear material & structure analysis suite. http://www.zset-software.com

[30] B Baufeld, M Bartsch, S Dalkilic, and M Heinzelmann. Defect evolution in thermal barrier coating systems under multi-axial thermomechanical loading. *Surface and Coatings Technology*, 200(5-6):1282–1286, Nov 21 2005.

[31] Frank M. White. *Heat and Mass transfer.* Addison-Wesley, 1988.

Table Click here to access/download;Table;Tables.docx

Tables

Table 1: Parameters of the three LASAT experiments

Shock number	Energy of laser (J)	Flux (GW)	Surface flux (GW/cm^2)
1	1.03	0.199	3.872
2	0.89	0.171	3.341
3	0.71	0.137	2.675

Table 2: Thermal properties for FE- analyses (from [29] for YSZ, TGO and BC properties and from [30] for air properties).

Material	T (K)	Conductivity (W/m/K)	Density 10^3 (kg/m^3)	Heat Capacity (J/kg/K)	Vol. Heat Capacity ($J/K/m^3$)
YSZ	RT	1.88	5	500	$2.50\ 10^6$
	1273	1.6	4.84	630	$3.05\ 10^6$
TGO	RT	23	4	769	$3.08\ 10^6$
	1273	5		1261	$5.04\ 10^6$
BC	RT	8.7	7.8	390	$3.04\ 10^6$
	1273	27.5	7.43	700	$5.20\ 10^6$
Air	250	0.0234	$1.20\ 10^{-3}$	1005	$1.21\ 10^3$
	1300	0.0804	$2.71\ 10^{-4}$	1197	$3.24\ 10^2$

Figure 1

Click here to access/download;Figure;Fig1_LASAT-diameter_neu.png

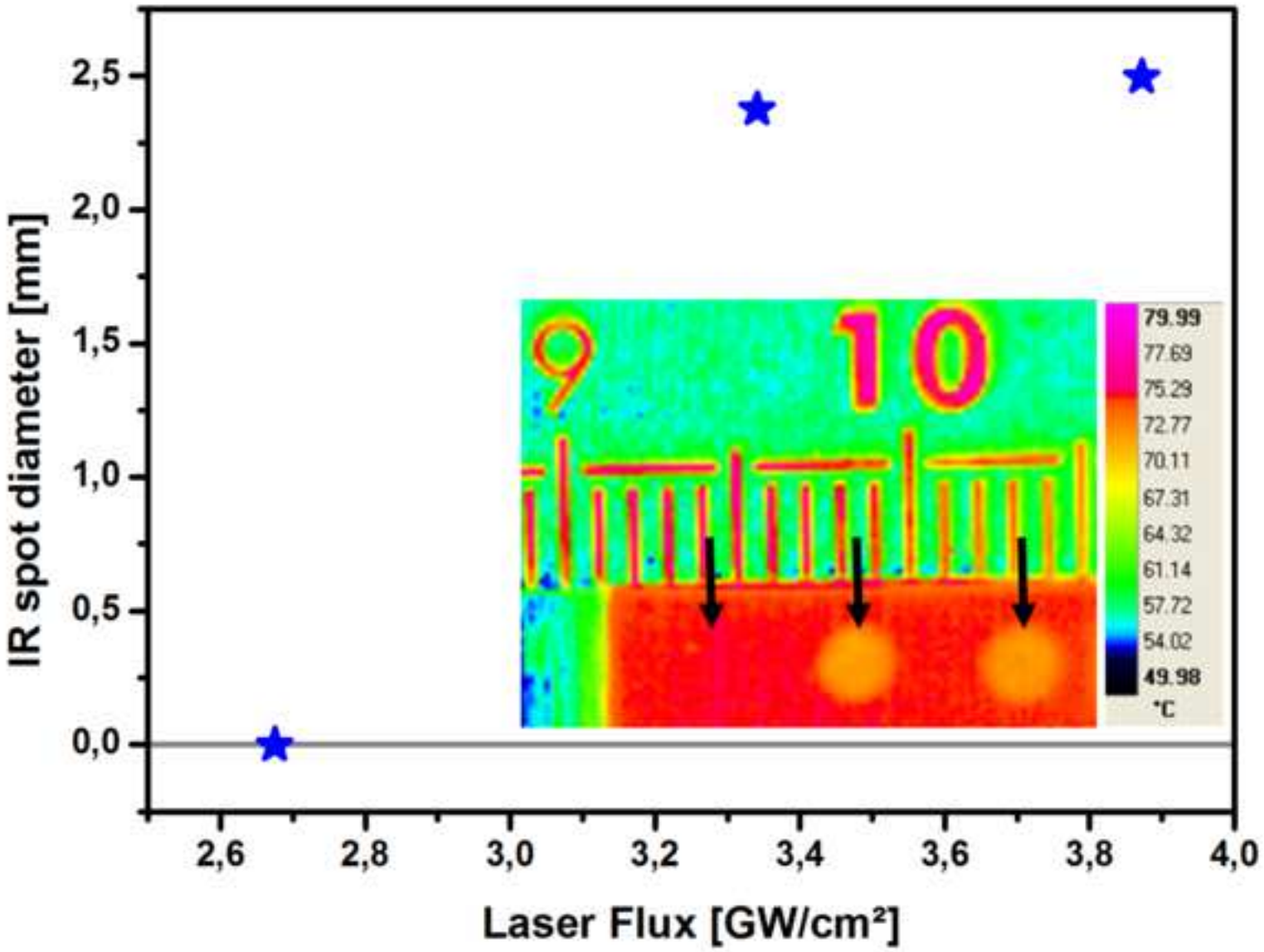

Figure 2a

Click here to access/download;Figure;Fig2_SEM-overview.tif

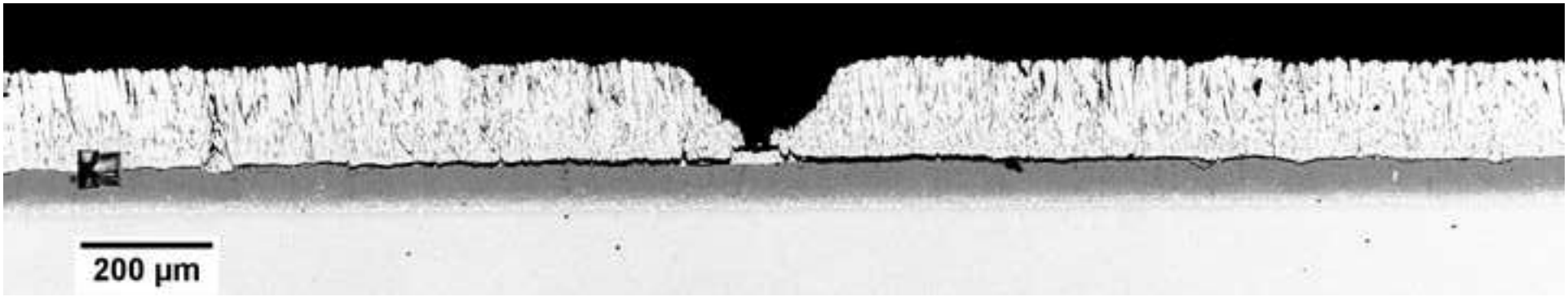

Figure 2b

Click here to access/download;Figure;fig2bschema.pdf

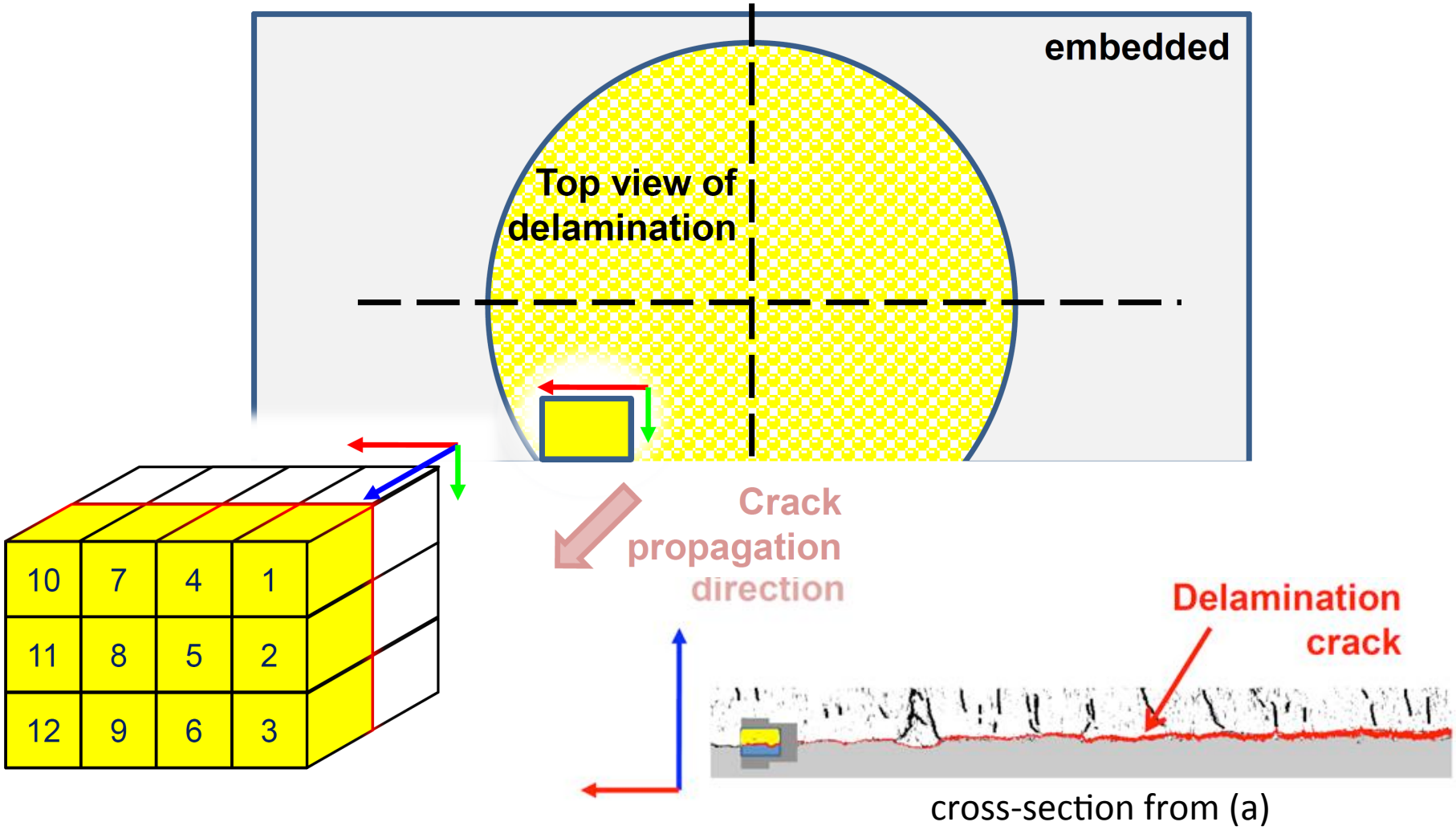

Figure 3a

Click here to access/download;Figure;Fig3-a_Volume_FIB171013_Mirror-image-stack_RBGG.png

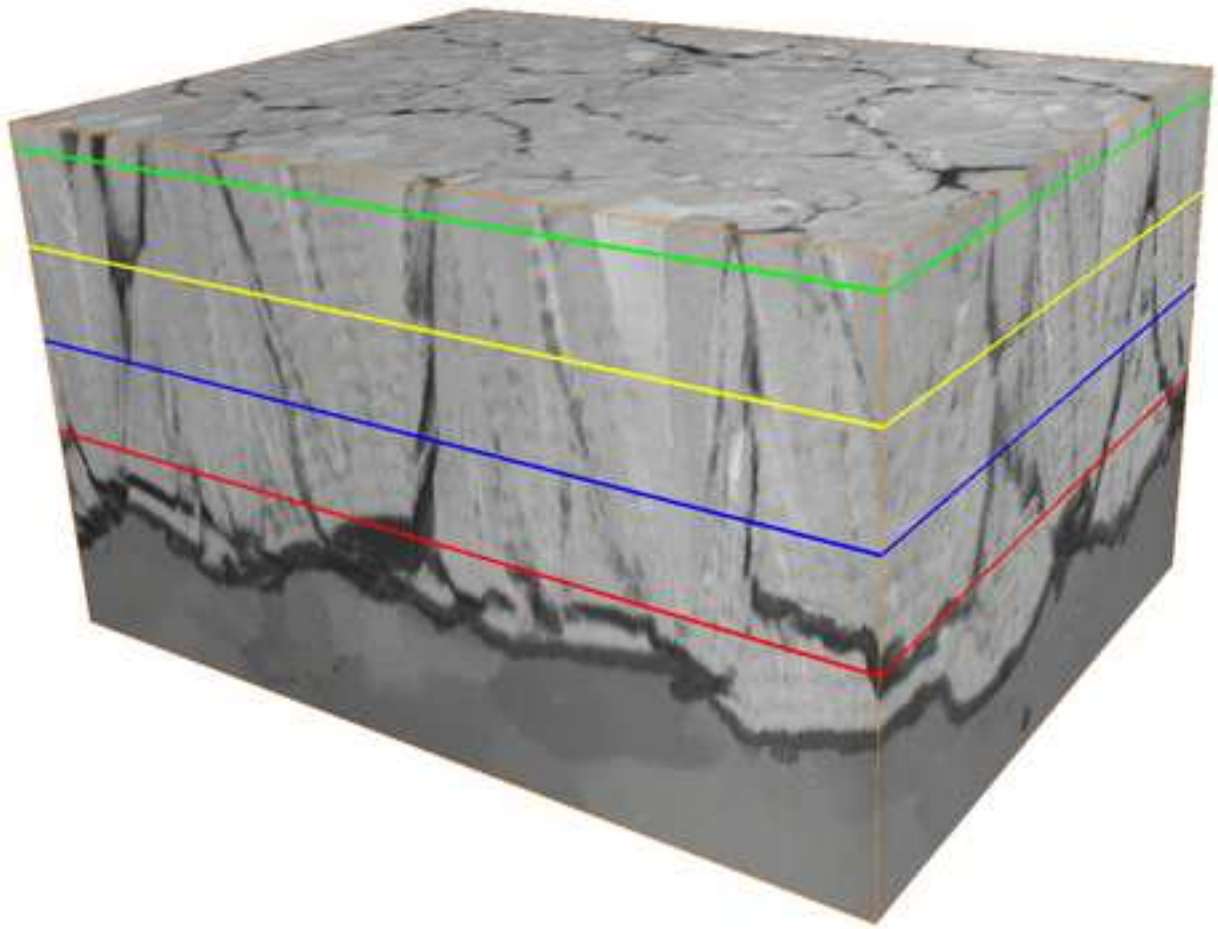

Avizo

Figure 3b

Click here to access/download;Figure;Fig3-b_ceramic-Slices_FIB171013.png

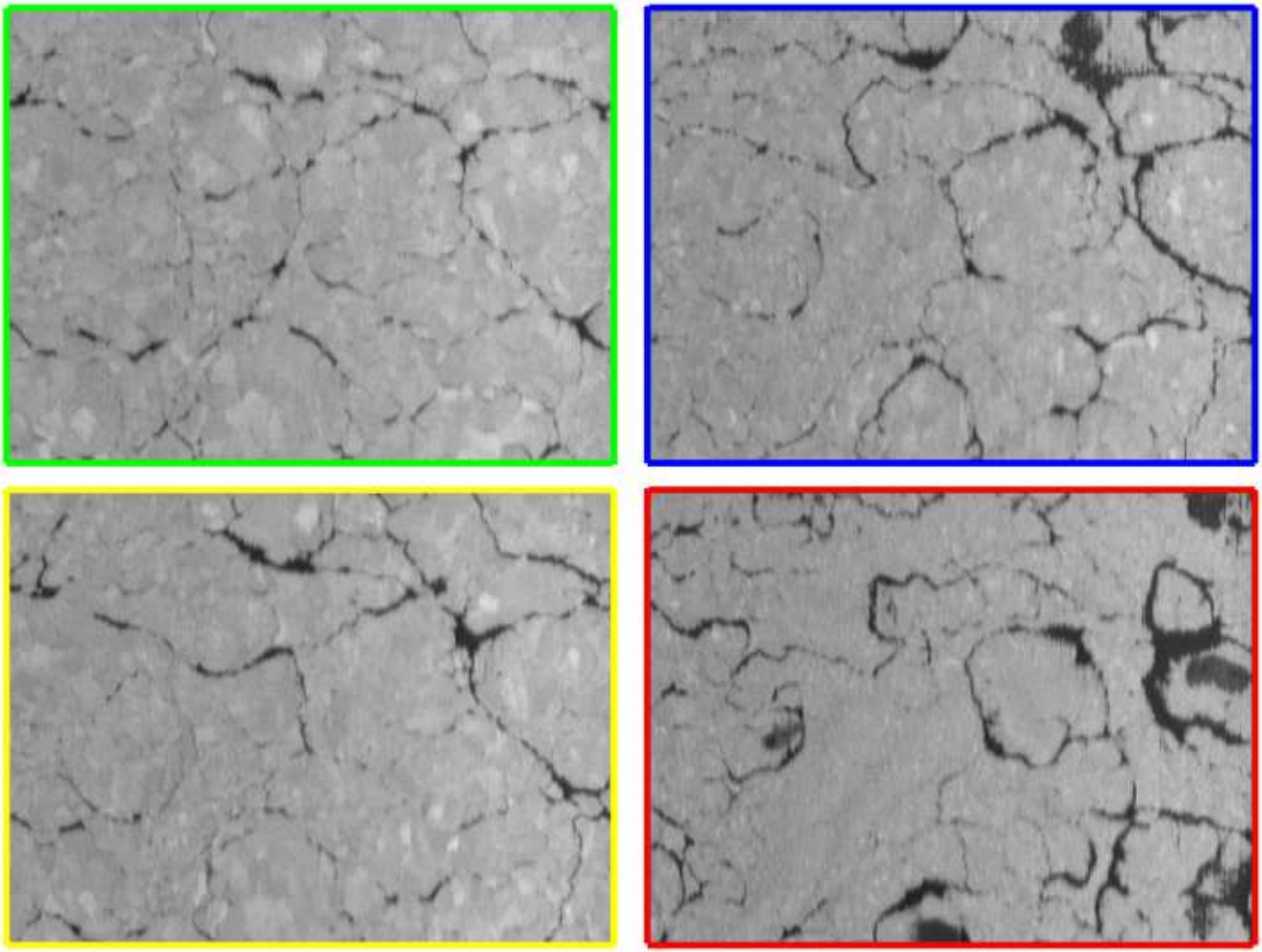

Figure 4a

Click here to access/download;Figure;Fig4-a_BSE-mode.tif

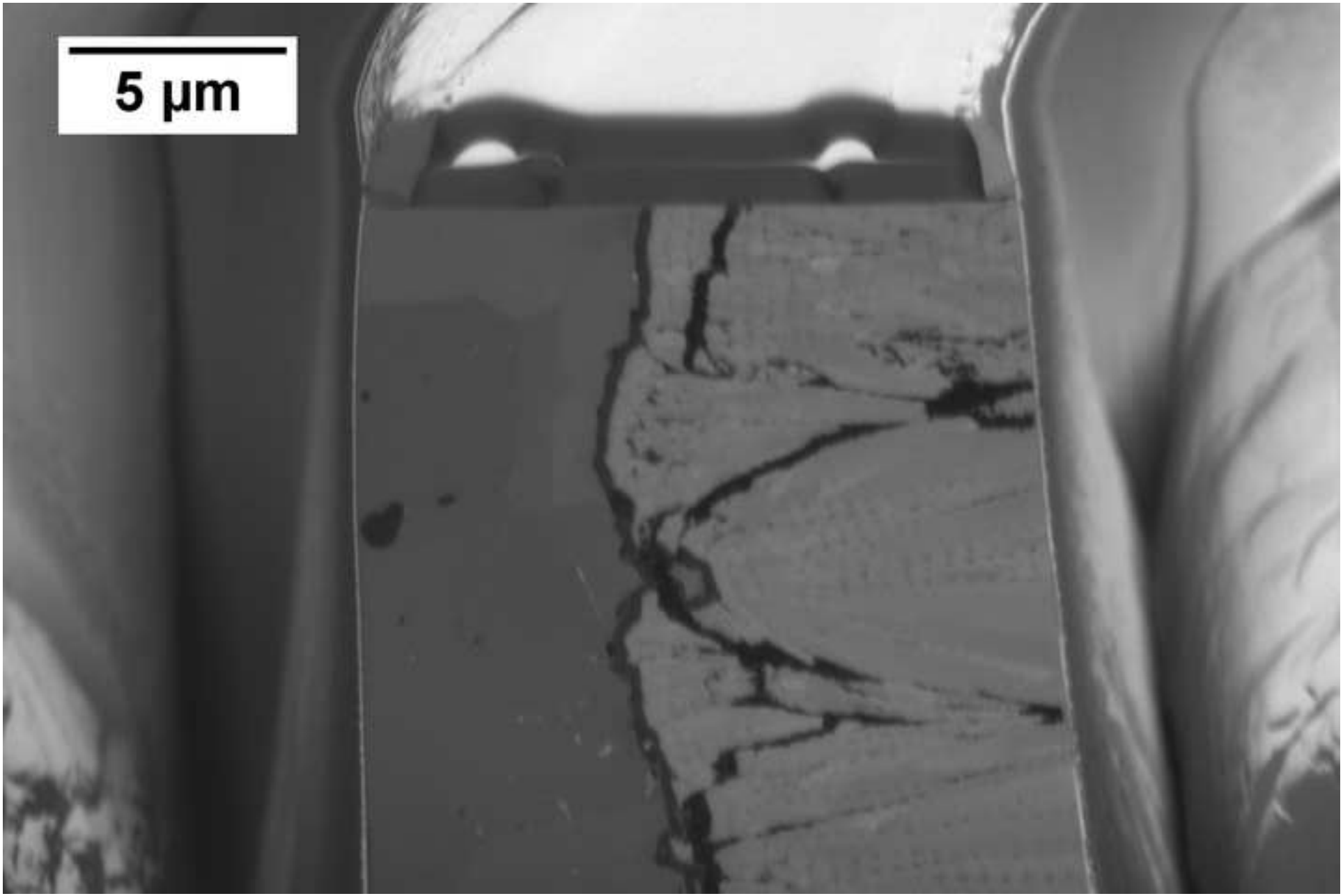

Figure 4b

Click here to access/download;Figure;Fig4-b_SE-mode.tif

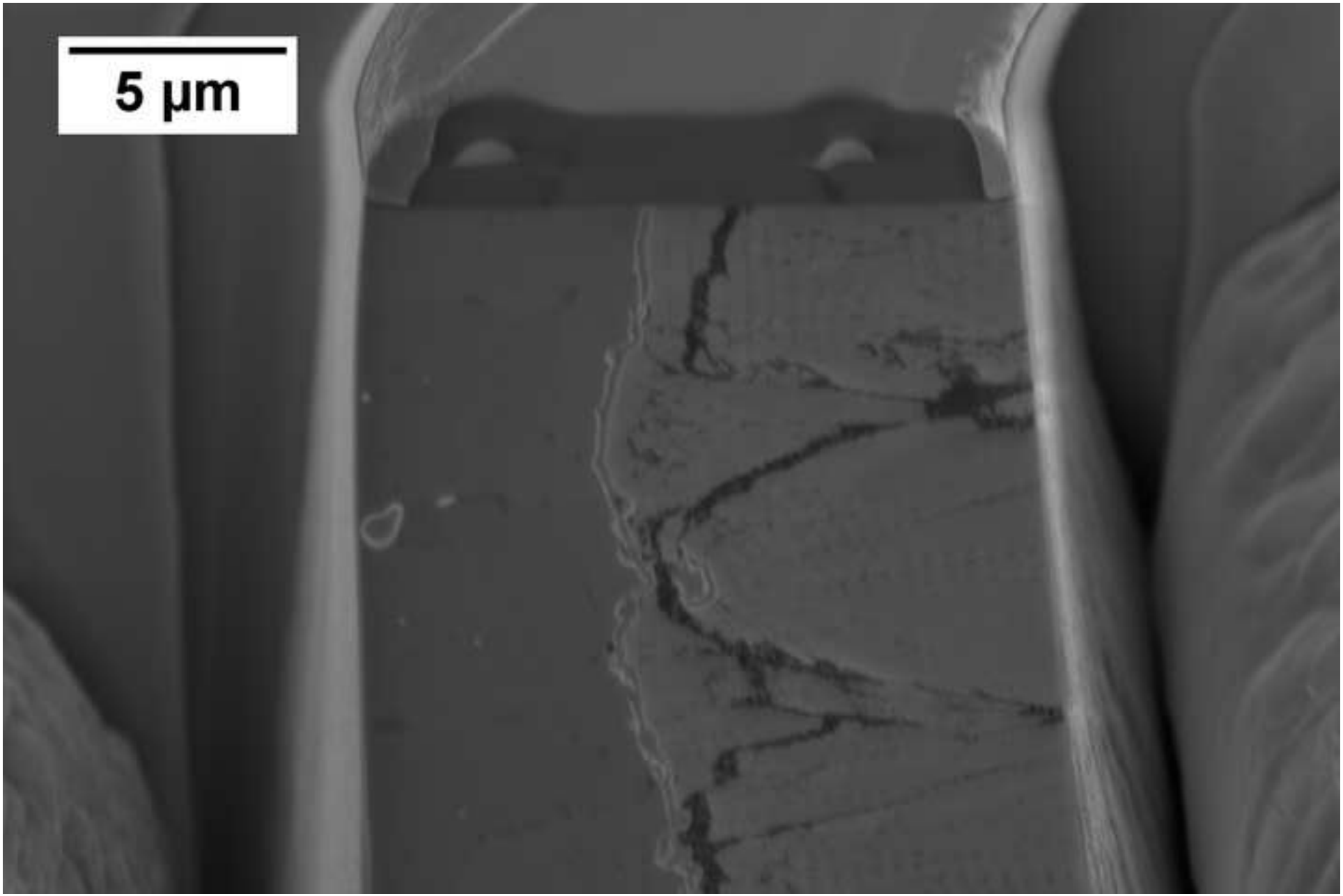

Figure 5

Click here to access/download;Figure;Fig5-Montage-Text-80.png

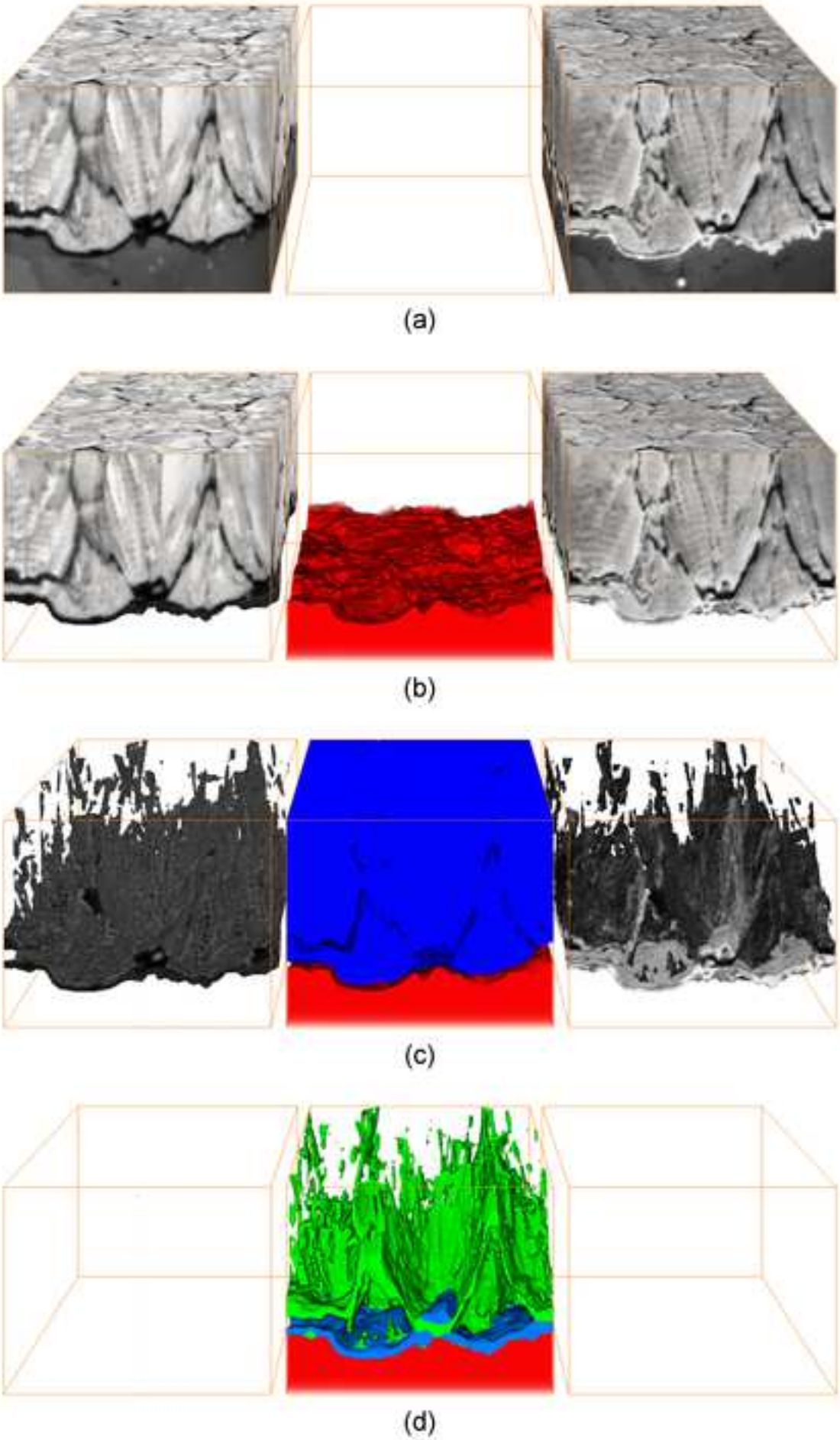

Figure 6

Click here to access/download;Figure;Figure_6.png

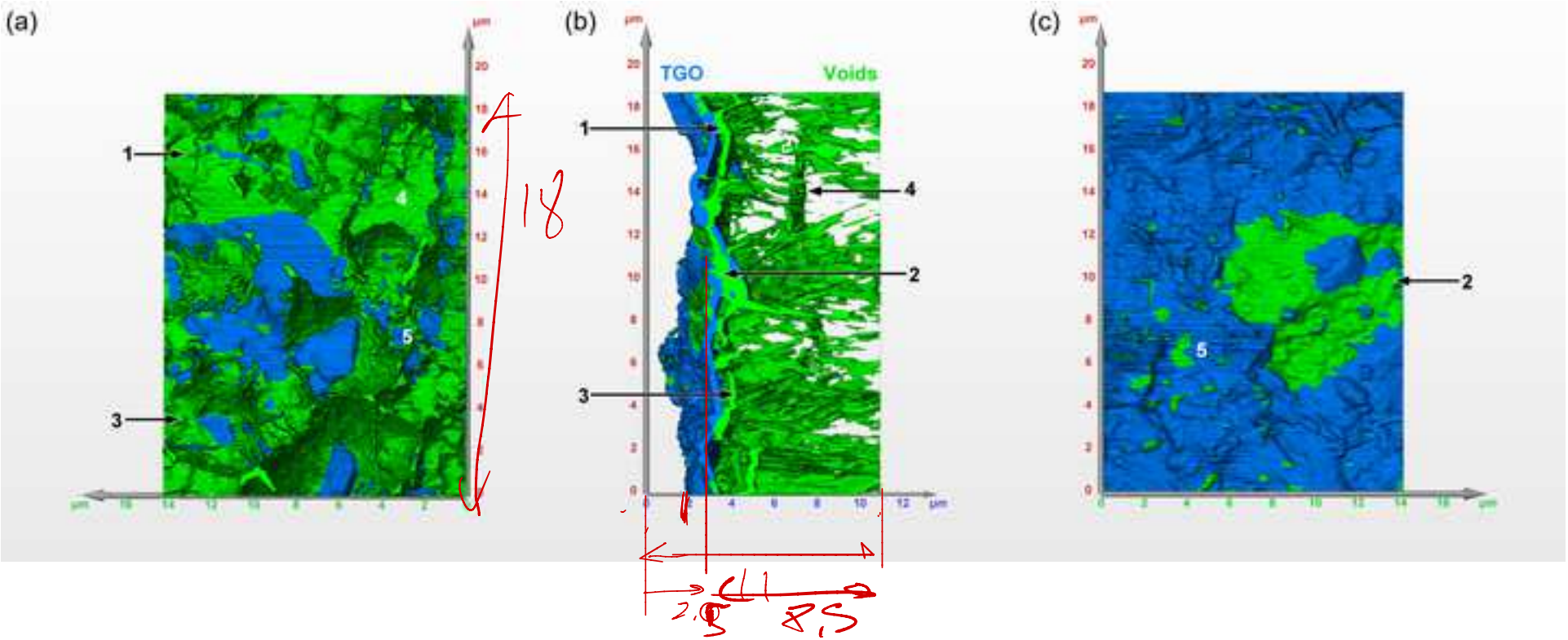

Figure 7

Click here to access/download;Figure;Figure_7.png

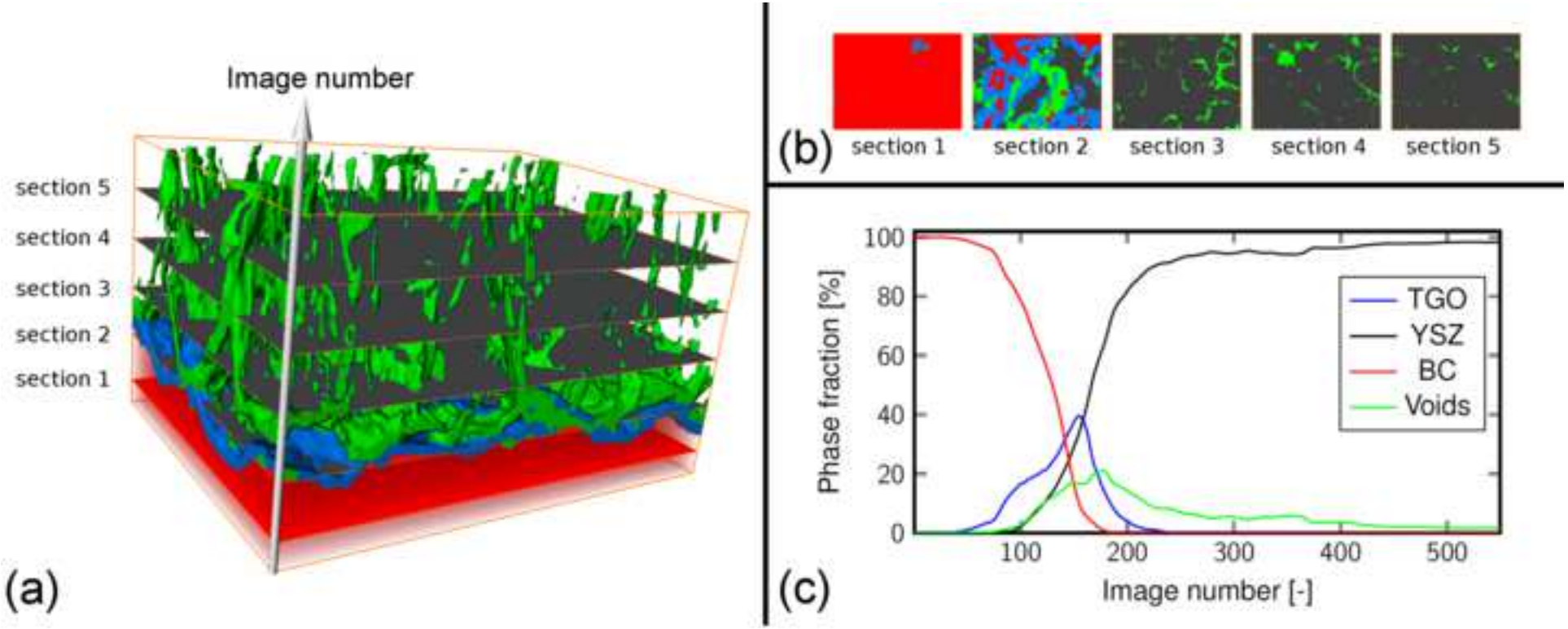

Figure 8

Click here to access/download;Figure;Figure_8.png

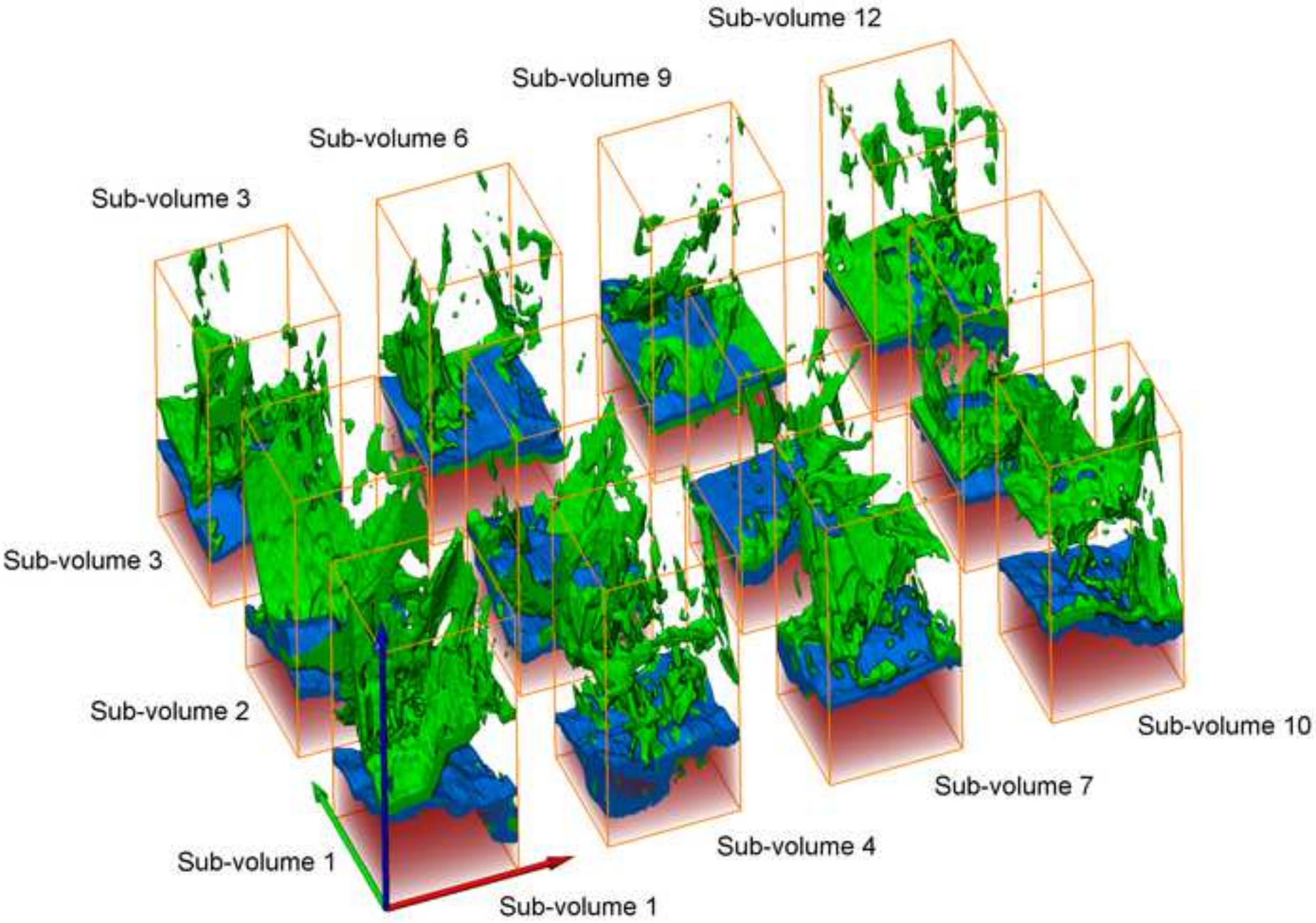

Figure 9

Click here to access/download;Figure;Figure_9.png

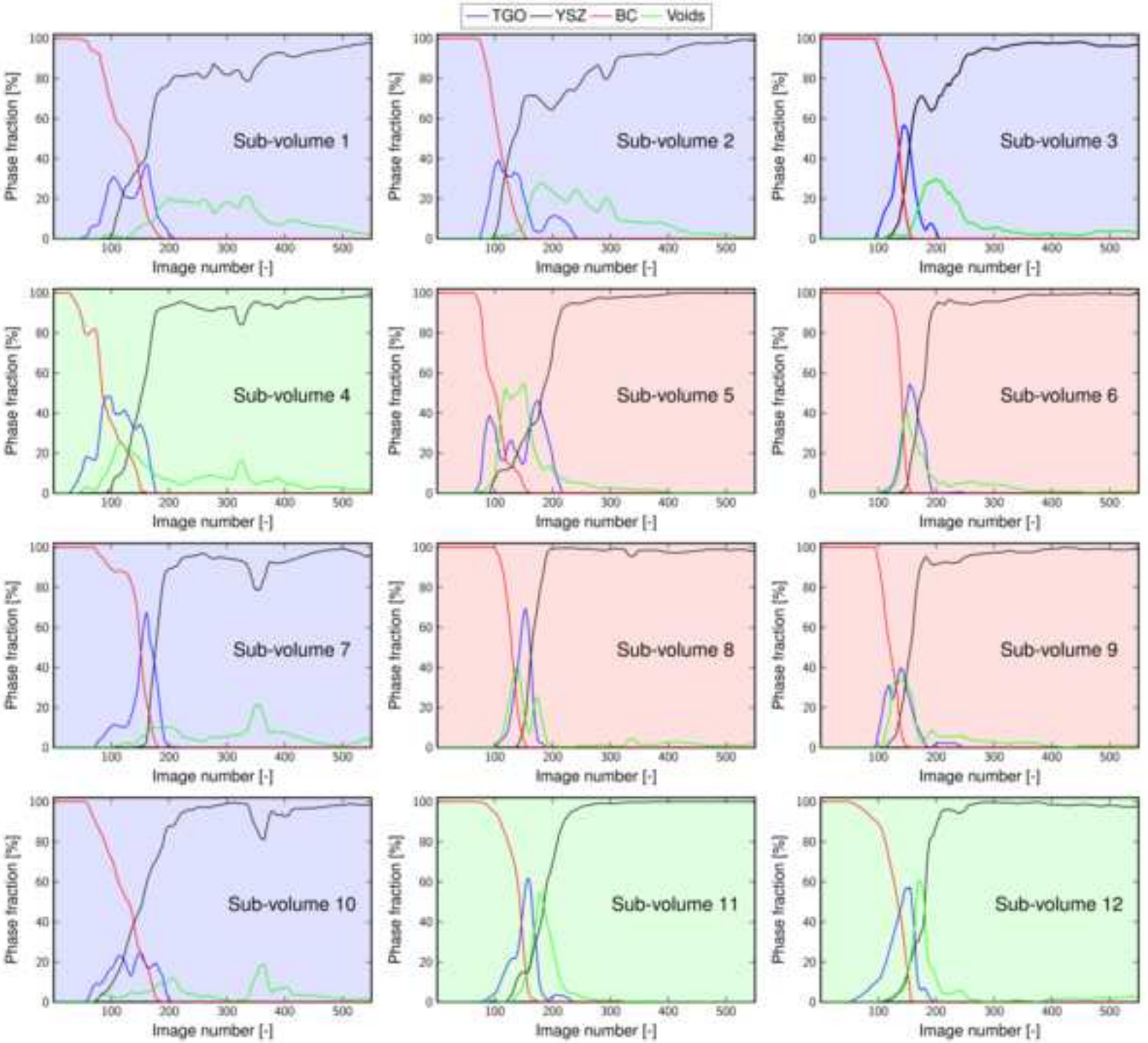

Figure 10

Click here to access/download;Figure;Figure_10.png

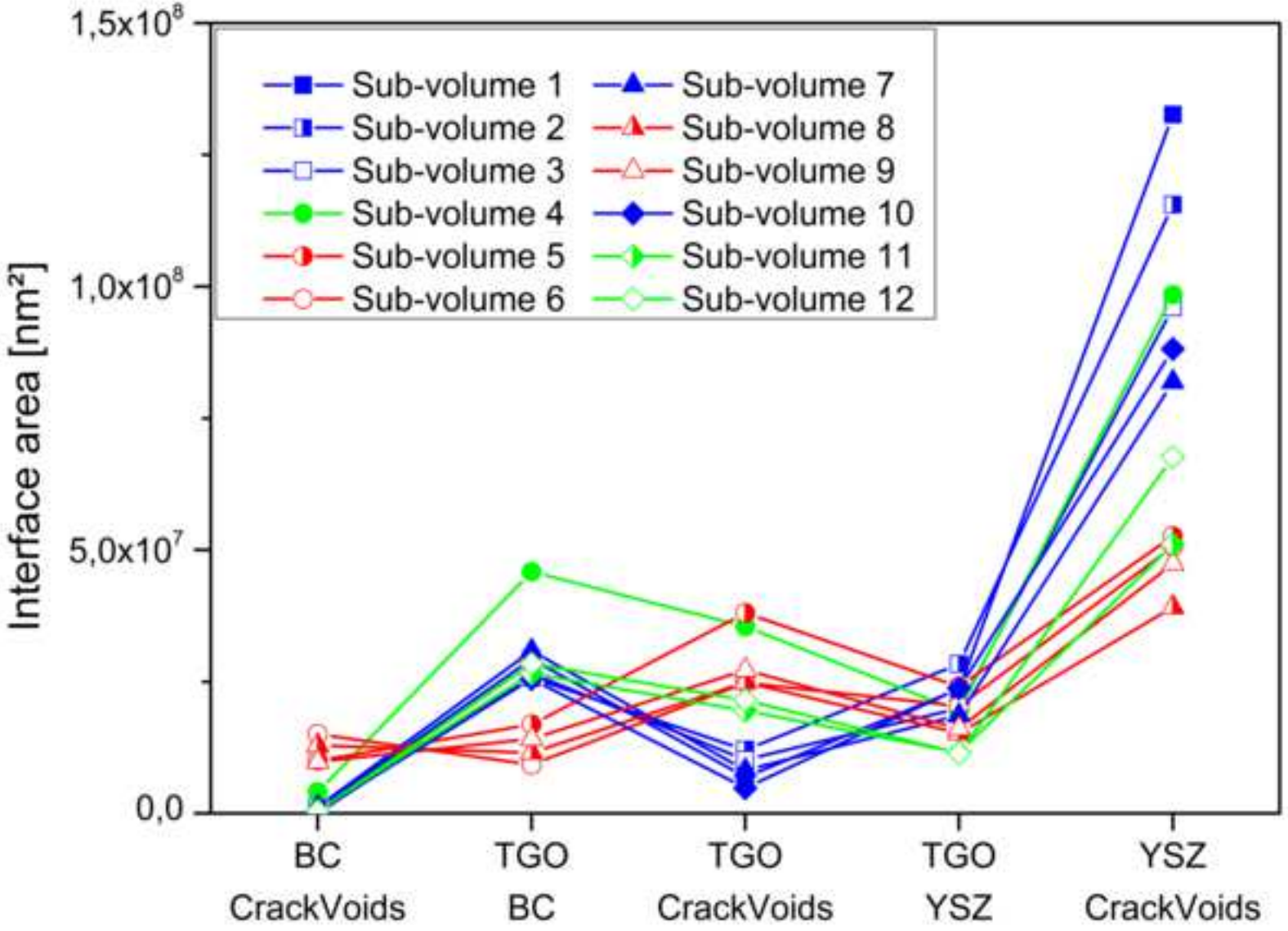

Figure 11

Click here to access/download;Figure;fig11FEAth_fieldabc.pdf

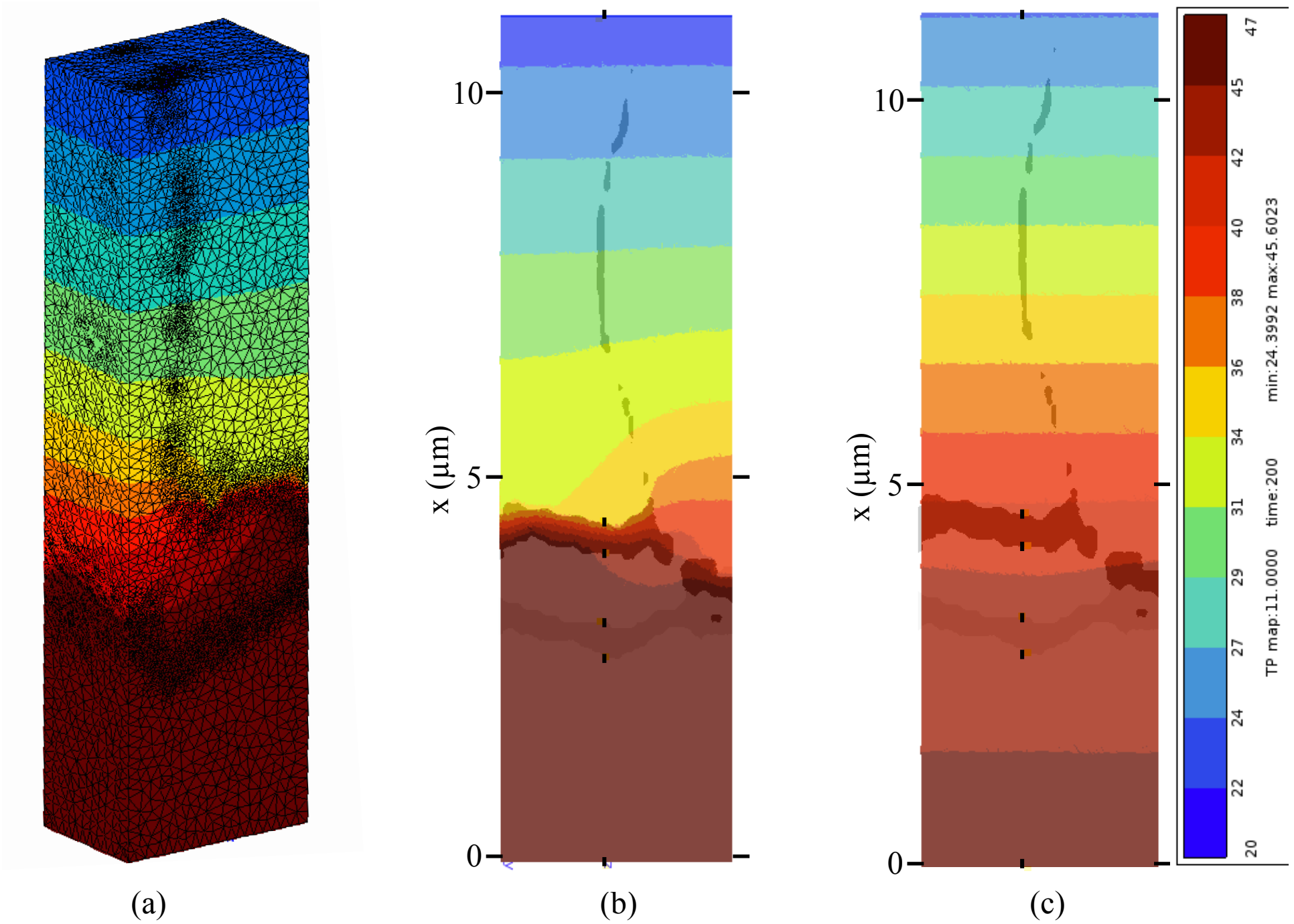

(a) (b) (c)

Figure 12a

Click here to access/download;Figure;fig12a_gradtherm_from1.eps

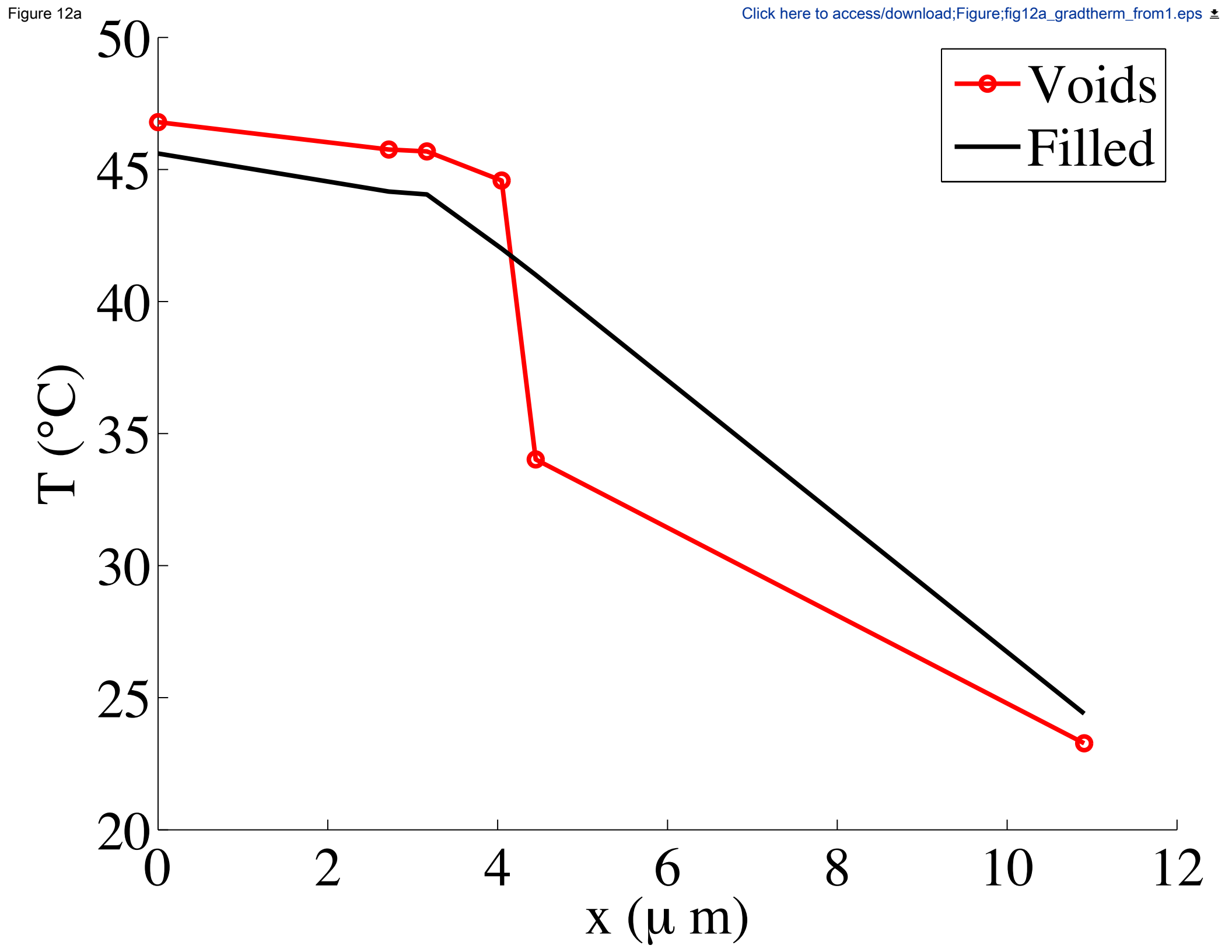

Figure 12b

Click here to access/download;Figure;fig12b_gradtherm_from2.eps